University of Louisville

ThinkIR: The University of Louisville's Institutional Repository

3-2005

The opacity of spiral galaxy disks. III. Automating the Synthetic Field Method.

Benne W. Holwerda
University of Louisville

R. A. Gonzalez
Universidad Nacional Autónoma de México

Ronald J. Allen
Space Telescope Science Institute

P. C. van der Kruit
University of Groningen

THE OPACITY OF SPIRAL GALAXY DISKS. III. AUTOMATING THE SYNTHETIC FIELD METHOD

B. W. Holwerda,[1,2] R. A. Gonzalez,[3] Ronald J. Allen,[1] and P. C. van der Kruit[2]

ABSTRACT

Dust extinction in spiral disks can be estimated from the counts of background field galaxies, provided the deleterious effects of confusion introduced by structure in the image of the foreground spiral disk can be calibrated. González et al. developed a method for this calibration, the Synthetic Field Method (SFM), and applied this concept to a *Hubble Space Telescope* (*HST*)/Wide Field Planetary Camera 2 image of NGC 4536. The SFM estimates the total extinction through the disk without requiring assumptions about the distribution of absorbers or disk light. The poor statistics, however, result in large errors in individual measurements. We report on improvements to and automation of the SFM that render it suitable for application to large archival data sets. To illustrate the strengths and weaknesses of this new method, the results on NGC 1365, an SBb galaxy, and NGC 4536, an SABbc, are presented. The extinction estimate for NGC 1365 is $A_I = 0.6^{+0.6}_{-0.7}$ at $0.45R_{25}$, and for NGC 4536 it is $A_I = 1.6^{+1.0}_{-1.3}$ at $0.75R_{25}$. The results for NGC 4536 are compared with those of González et al. The automation is found to limit the maximum depth to which field galaxies can be found. Taking this into account, our results agree with those of González et al. We conclude that this method can only give an inaccurate measure of extinction for a field covering a small solid angle. An improved measurement of disk extinction can be done by averaging the results over a series of *HST* fields, thereby improving the statistics. This can be achieved with the automated method, trading some completeness limit for speed. The results from this set of fields are reported in a companion paper by Holwerda et al.

Key words: astronomical data bases: miscellaneous — dust, extinction —
galaxies: individual (NGC 1365, NGC 4536) — galaxies: ISM — galaxies: photometry —
galaxies: spiral — methods: statistical — radiative transfer — techniques: photometric

Online material: color figures

1. INTRODUCTION

The question of how much the dust in spiral galaxies affects our perception of them became a controversial topic after Valentijn (1990) claimed that spiral disks were opaque. Valentijn based his conclusion on the apparent independence of disk surface brightness on inclination. Disney (1990) objected to this conclusion, claiming instead that galaxy disks are virtually transparent and that Valentijn's results were due to a selection effect. Others joined the controversy, and within a few years a conference was organized to address the question of how best to determine galaxy disk opacity and what results could be obtained (Davies & Burstein 1995).

Notably, White & Keel (1992) proposed a method to determine the opacity of a foreground disk galaxy in the rare cases where it partially occults another large galaxy. This technique has been followed up extensively with ground-based optical and infrared imaging (Andredakis & van der Kruit 1992; Berlind et al. 1997; Domingue et al. 1999; White et al. 2000), spectroscopy (Domingue et al. 2000), and *Hubble Space Telescope* (*HST*) imaging (Keel & White 2001a, 2001b; Elmegreen et al. 2001). The results by White & Keel indicated higher extinction in the arms and a radial decrease of extinction in the interarm regions. In addition, the highest dust extinction was found in the areas of high surface brightness. Their sample of ~20 suitable

pairs seems now to be exhausted. This method furthermore assumes symmetry for the light distribution of both galaxies, so that a method independent of the light distribution is needed to confirm the results.

Instead of a single large background galaxy, the general field of distant galaxies can be used as a background source. Hubble (1934) noted the apparent reduction in the surface density of background galaxies at lower Galactic latitudes. Burstein & Heiles (1982) published a map of Galactic extinction based on the galaxy counts by Shane & Wirtanen (1967). Studies of extinction in the Magellanic clouds based on field galaxy counts have been done regularly (Shapley 1951; Wesselink 1961; Hodge 1974; MacGillivray 1975; Gurwell & Hodge 1990; Dutra et al. 2001). More recently, attempts have been made to use field galaxy counts in order to establish the opacity in specific regions of nearby foreground galaxies from ground-based data (Zaritsky 1994; Lequeux et al. 1995; Cuillandre et al. 2001). Occasionally, the presence of field glaxies in a spiral disk is presented as anecdotal evidence of galaxy transparency (Roennback & Shaver 1997; Jablonka 1998). The results of these studies suffer from the inability to distinguish real opacity from foreground confusion as the reason for the decrease in field galaxy numbers.

González et al. (1998, hereafter Paper I) introduced a new approach to calibrate foreground confusion which they called the Synthetic Field Method (SFM). While this new method can provide the required calibration for specific foreground galaxies, it is labor intensive and therefore ill suited to the study of larger samples of galaxies of various types. In this paper we present the first results from a project to automate major steps in the SFM. After first providing a brief summary of the major features of the method, we describe how it was automated

[1] Space Telescope Science Institute, 3700 San Martin Drive, Baltimore, MD 21218; holwerda@stsci.edu.
[2] Kapteyn Institute, Groningen Landleven 12, NL-9747 AD Groningen, Netherlands.
[3] Centro de Radioastronomía y Astrofísica, Universidad Nacional Autónoma de México, 58190 Morelia, Michoacán, Mexico.

and what improvements we have made. As an illustration we applied the new automated method to two galaxies, NGC 4536 and NGC 1365, and compared the results of our improved algorithms with those obtained on the former galaxy by Paper I. In a companion paper (Holwerda et al. 2005, hereafter Paper IV) we report on our application of the method to a data set consisting of 32 *HST*/Wide Field Planetary Camera 2 (WFPC2) pointings on 29 nearby galaxies.

2. THE SYNTHETIC FIELD METHOD

Figure 1 shows a schematic of how the SFM is applied. Deep exposures of a nearby galaxy are obtained with the WFPC2 on *HST*, and background field galaxies are identified. Synthetic fields are then created by adding exposures from the Hubble Deep Fields (HDFs; Williams et al. 1996, 2000), and the background field galaxy counts are repeated. The ratio of the surface density of real field galaxies to that of the HDF galaxies for any given region is a measure of the opacity in that region of the foreground galaxy. In practice, a series of synthetic fields is created with successively larger extinctions applied to the HDF galaxies until a match is obtained with the real field-galaxy count, thus providing a quantitative measure of opacity in the foreground system. The method provides a way of calibrating the deleterious effects of confusion caused by the granular structure of dust, stars, and luminous gas in the foreground galaxy. These effects are dramatic; for example, a typical single WFPC2 chip ($1\farcm2 \times 1\farcm2$) in the HDF may contain some 120 easily identified background galaxies. This can drop to only 20 or 30 HDF galaxies when the foreground galaxy is present, and this number becomes even smaller for the larger values of a simulated foreground opacity. Counting background galaxies is therefore a battle against small number statistics, and reliable results are difficult to obtain on a single foreground galaxy. However, the method can in principle be applied to many nearby galaxies and average opacities obtained, e.g., as a function of radius for a sample of galaxies of similar morphological type.

2.1. *Limits of the Synthetic Field Method*

González et al. (2003) discussed the broad limitations of the method in terms of the optimum distance interval for which it can be used most effectively, given current and future ground- and space-based imaging instruments. Two effects compete to limit the distance to which the SFM can be applied: First, if the foreground galaxy is too close, confusion from the granularity in the images caused by a more resolved foreground disk further reduces the number of bona fide field galaxies. Second, if the foreground galaxy is too distant, the small area of sky covered also reduces the number of field galaxies that can be used. These two effects conspire, such that the optimum distance range for the SFM with *HST*/WFPC2 observations is approximately between 5 and 25 Mpc. Within this range there are of course many hundreds of galaxies visible to *HST*. However, now we are hindered by another limitation of the specific implementation of the SFM used by Paper I, namely, that the identification of background and synthetic galaxies was carried out entirely visually, a time-consuming and laborious process. Clearly, if any real progress is to be made, the process of identifying the field galaxies has to be automated (Holwerda et al. 2001, 2002a). Automated field-galaxy identification has the benefits of speed and consistency across the data sets. Conversely, in § 5.1 we illustrate how it imposes a brightness limit on the selected objects.

3. AUTOMATION OF THE METHOD

We automated three steps in the SFM: first, the processing of archived exposures to produce combined images; second, the construction of catalogs of objects of simulated and science fields; and, finally, the automatic selection of candidates for field galaxies based on the parameters in the catalogs. A visual control on the process was retained by reviewing the final list of candidate field galaxies in the science field. We now describe each step in the entire process in more detail.

3.1. *Processing Archival WFPC2 Data*

When data sets are recovered from the *HST* archive, the most recent corrections for hot pixels, bad columns, geometric distortions, and the relative Wide Field (WF) and the Planetary Camera (PC) CCD positions for the observation date are applied in the archive's pipeline reduction. This pipeline system provides the user with a science data file and a quality file with positions of the bad pixels (Swam & Swade 1999).

In order to stack multiple exposures, corrected for small position shifts and with the cosmic rays removed, we used the "drizzle" method (Mutchler & Fruchter 1997), packaged in routines under IRAF/*pyraf*, with an output pixel scale of 0.5 of the original pixel and PIXFRAC between 0.8 and 1.0, depending on the number of shifts in the retrieved data. The PIXFRAC parameter sets the amount by which the input pixel is shrunk before it is mapped onto the output plane; a PIXFRAC lower than unity improves the sampling of the stacked image.

We developed a custom script to combine all exposures using *python* with the *pyraf* package (Greenfield & White 2000), on the basis of examples in the Dither Handbook (Koekemoer 2002). The images are prepared for cross-correlation in order to find the relative shifts; the background was subtracted (*sky*) and all none-object pixels were set to zero (*precor*). Subsequently, cross-correlation images between exposures were made for each of the four CCDs (*crosscor*). The fitted shifts from these were averaged (*shiftfind*, *avshift*). Any rotation of an exposure was calculated from the header information and ultimately derived from the spacecraft orientation provided by the guide stars.[4] All original exposures were shifted to the reference coordinates, and a median image was constructed from these (*imcombine*). The median image was then copied back to the original coordinates (*blot*). The cosmic rays in each exposure were identified from the difference between the shifted median image and the original exposure (*driz_cr*). A mask with the positions of the cosmic rays and hot pixels, identified in the data quality file, was made for each exposure.

The exposures were drizzled onto new images and separately onto a mosaic with cosmic rays and bad pixels masked off (*drizzle*, *loop_gprep*). The new pixel scale is fixed at $0\farcs05$, but to check the choice of PIXFRAC value, the script computed the rms of the weight image output from drizzle. The rms standard deviation should be between 15% and 30% of the mean.

For both galaxies used as examples here, there are many exposures made over several epochs. However, the shifts for NGC 4536 are smaller than 1 original pixel ($0\farcs1$), and the bad columns of the CCD detector are unfortunately not covered by good pixels from other exposures (see Fig. 2). Several exposures for NGC 1365 display shifts greater than a pixel, which

---

[4] The uncertainty in the orientation angle is the result of uncertainties of a few arcseconds in the positions of guide stars with a separation of a few arcminutes. Therefore, this uncertainty is an order of magnitude smaller than the uncertainties in right ascension and declination of the pointing.

Step1: Identify field galaxies in the data.
Step2: Combine data with extincted HDF.
Step3: Identify galaxies in simulations.
Step4: Compare numbers of real and
        simulated galaxies.
Step5: Measured opacity is the intersection
        of the real number with the line
        of simulations.

(2)

Data   Simulation

Original Image

Simulated Dust

Hubble Deep Field

(4)

(3)
Number of simulated galaxies
as a function of simulated
dust opacity.

(1)
Number
of real
field galaxies
(constant).

(5) Best estimate of field opacity
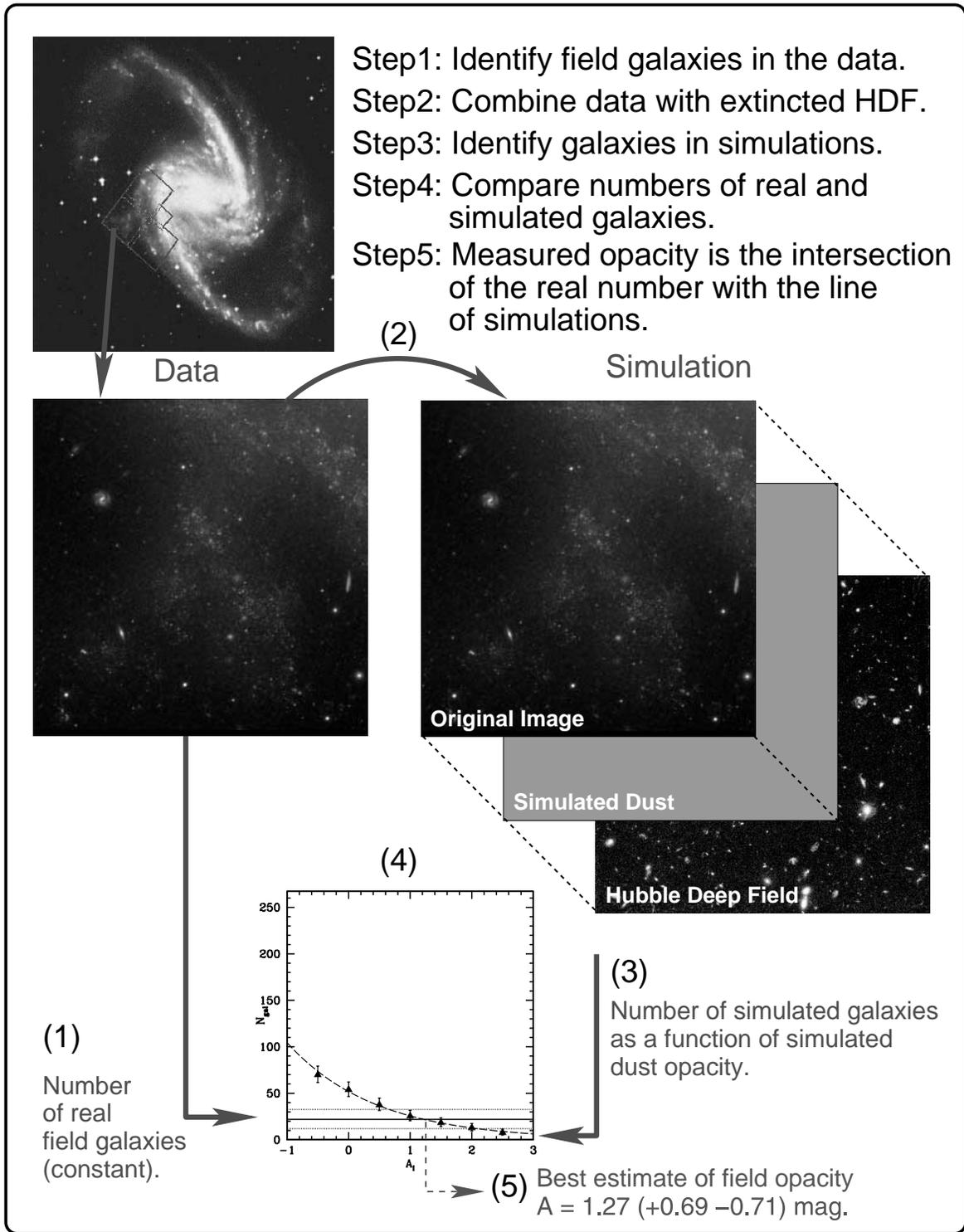A = 1.27 (+0.69 −0.71) mag.

Fig. 1.—Schematic of the SFM. First, field galaxies are identified in the science field by a combination of automatic and visual selection. Second, an HDF field is added to the science field in a series of simulations with different opacities. Field galaxies are selected from these simulated fields. Eq. (3) is fitted to these, and uncertainties are estimated. Finally, the intersection between that relation and the number of galaxies gives the opacity of the area under consideration. In this case, the WF3 chip of NGC 1365 has an average extinction of $1.3^{0.7}_{-0.7}$ mag.
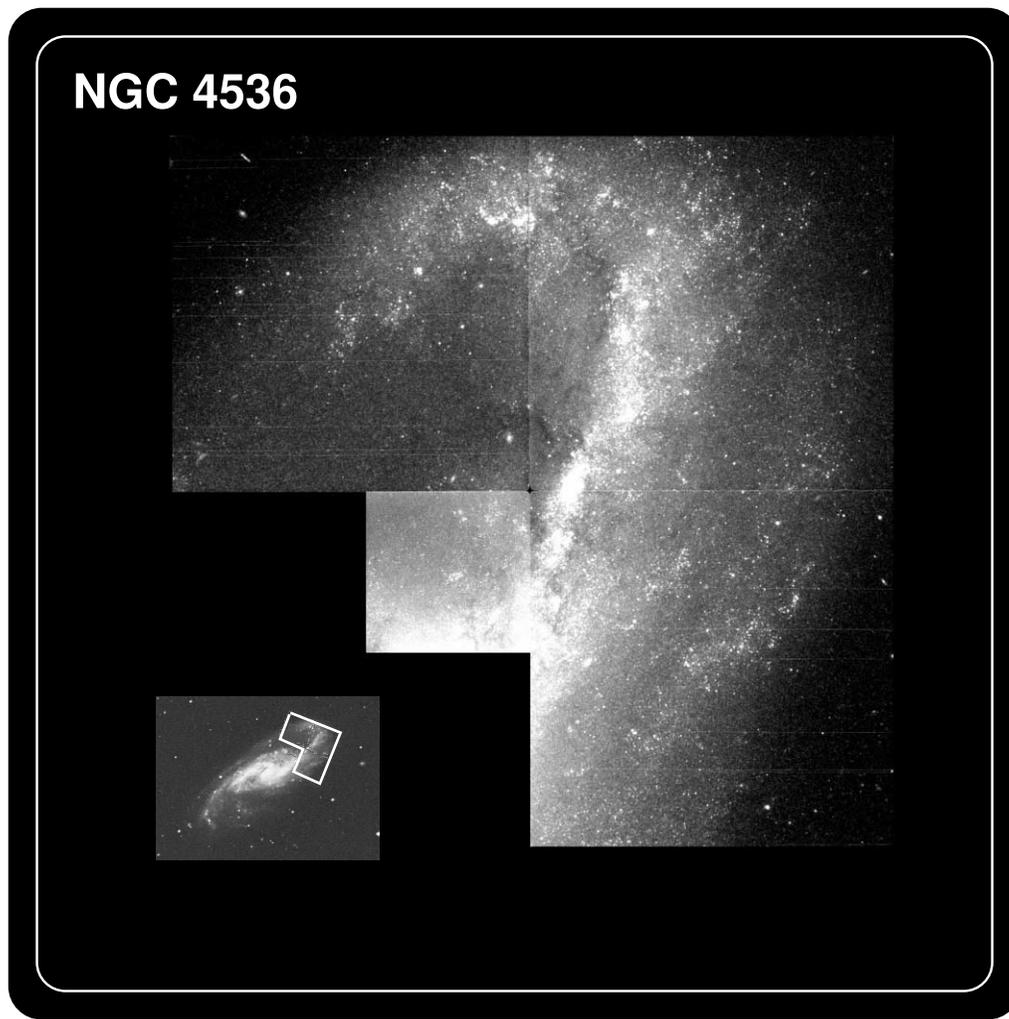
F_{IG.} 2.—Mosaic made of the *HST*/WFPC2 exposure of the northeast arm of NGC 4536; the inset is the Digital Sky Survey image with the WFPC2 footprint. Because of the lack of a dither greater than 1 pixel between epochs, some of the effects of masked bad columns can still be seen.

helps to cover the bad columns and results in a cleaner looking image (Fig. 8). In both cases the number of shifts was sufficient for a PIXFRAC of 0.8, with the new pixel scale of 0″.05.

3.2. *Making Object Catalogs*

A modified version of Source Extractor v2.2.2 (SE; Bertin & Arnouts 1996) was used to generate catalogs of objects for the science fields and simulations. The F814W (*I*-band) fields were used for detection. Catalogs for the F555W (*V*-band) fields were constructed using the dual mode; the photometry was done on the *V* field using the *I* apertures. All the structural parameters were derived from the *I* images. In Table 1 we list our choice of SE input settings. Table 2 lists the intrinsic output parameters from SE, and Table 3 the new output parameters we added. In addition, the position of objects on the CCD and on the sky are in the catalogs.

It was already noted by Bertin & Arnouts (1996) that the success of SE's native star/galaxy classification parameter was limited to the very brightest objects. Several other parameters are described in the literature for the classification of field galaxies. Abraham et al. (1994, 1996a, 1996b) used asymmetry, contrast, and concentration to identify the Hubble type of galaxies. Similarly, Conselice (1997, 1999, 2003), Conselice et al. (2000), and Bershady et al. (2000) used asymmetry, concen-

tration, and clumpiness as classifiers. By adding some of these parameters or our approximations of them to the SE code, we obtained a better parameter space within which to separate field galaxies from objects in the foreground galaxy.

3.3. *Selection of Field Galaxy Candidates Using "Fuzzy Boundaries"*

The characteristics as determined by SE for field galaxies and foreground objects are very similar; for example, we show in Figure 3 the distribution of the FWHM of all objects and that of the HDF galaxies. This similarity exists because there are many extended foreground objects: star clusters, H II regions, artifacts from dust lanes, diffraction spikes near bright stars, and "objects" that are actually blends of several objects. The field galaxies also span a range in characteristics, as can be seen in the HDFs. Simple cuts in parameter space can do away with some objects that are clearly not field galaxies, but the field galaxies cannot be uniquely selected that way.

In order to select objects most likely to be field galaxies, we developed a fuzzy-boundary selection method. From a training set of objects with known field galaxies, the fraction of field galaxies in a bin of a relevant SE output parameter can be determined. Our training set consists of catalogs of the simulations with no artificial extinction of five galaxies in our sample

TABLE 1
SOURCE EXTRACTOR INPUT PARAMETERS

Parameter	Value	Comments
PIXEL_SCALE......................................	0.05	Scale in arcseconds after drizzling
SEEING_FWHM..................................	0.17	FWHM of the *HST* PSF
BACK_SIZE......................................	32	Background estimation anulus
BACK_FILTERSIZE............................	3	Background estimation smoothing factor
BACKPHOTO_TYPE	LOCAL	Photometric background
BACKPHOTO_THICK	32	Photometric background anulus
DETECT_MINAREA............................	10	Minimum number of pixels in object
FILTER	Y	Smooth before detection?
FILTER_NAME...................................	gauss_4.0_7x7.conv	Smoothing kernel, Gaussian with 4 pixel FWHM
DEBLEND_NTHRESH..........................	32	Number of deblending thresholds
DEBLEND_MINCONT	0.001	Deblending minimum contrast
CLEAN	Y	Remove bright object artifacts?
CLEAN_PARAM	1.5	Moffat profile β used for cleaning
PHOT_APERTURES.............................	3, 5, 11, 21, 31	Fixed aperture diameters
GAIN..	7.0	Gain of the WF CCD

(NGC 1365, 2541, 3198, 3351, and 7331). In these catalogs, the added HDF galaxies were identified by their positions.[5] The fraction of HDF galaxies in a SE parameter bin can then be used as a probability that an unknown object with a value in that bin is a field galaxy. By multiplying these fractions of HDF galaxies for every relevant SE parameter (P_i) for each object, an overall galaxy-likeness score (P) for that object is obtained:

$$P = \left\{ \frac{\prod P_i}{(\prod P_i) + [\prod (1 - P_i)]} \right\}. \quad (1)$$

We used the distribution of the log of these probabilities ($\log P$) as a sliding scale of the galaxy-like quality of an object. The distribution of $\log P$ for objects in 21 science fields is plotted in Figure 4, with the distribution of HDF-N/S objects

scaled for comparison. The advantage of using an overall scale is that an object can fare poorly for one SE parameter but still make the selection. This makes the boundaries for any single parameter in parameter space of the field galaxies fuzzy.[6] All the structural parameters marked in Tables 2 and 3, as well as the $V - I$ color from the smallest aperture, were used in computing the galaxy score. The selection criterion is an overall score ($\log P$) greater than the log of the mean score of all objects plus 2.5, that is:

$$\log P > \log P_{\mathrm{mean}} + 2.5. \quad (2)$$

_____

[5] The training set was identified by their positions. The selection of field galaxies was based on their properties, not their position.

[6] This resembles a Bayesian approach to the classification problem, first applied to star/galaxy separation by Sebok (1979). The parameters we use, however, are not completely independent of each other, and the HDF percentages represent an underestimate of the chances, as the real galaxies in the bins are not considered field galaxies, but other objects, skewing the ratio slightly. This scoring system, however, worked well in practice for the selection of field galaxy candidates.

TABLE 2
SOURCE EXTRACTOR INTRINSIC OUTPUT PARAMETERS

Name	Description	Unit	Used	Comments
A_IMAGE.....................................	Major axis	pixel	*	
B_IMAGE.....................................	Minor axis	pixel		a
ELLIPTICITY................................	1 - B_IMAGE/A_IMAGE	...	*	
FWHM_WORLD..........................	FWHM assuming a Gaussian core	deg	*	
FLUX_RADIUS	Fraction-of-light radii	pixel	*	b
ISOAREA_IMAGE	Isophotal area above analysis threshold	pixel^2	*	
CLASS_STAR	S/G classifier output	...	*	c
MAG_ISO.....................................	Isophotal magnitude	mag		d
MAG_AUTO	Kron-like elliptical aperture magnitude	mag		
MU_MAX.....................................	Peak surface brightness above background	mag arcsec^{-2}	*	e
MAG_APER.................................	Fixed aperture magnitude vector	mag	*	f

[a] B_IMAGE was not used in the calculation of the galaxy score. The information is already contained in A_IMAGE and ELLIPTICITY.

[b] FLUX_RADIUS is the radius in pixels containing a given percentage of the flux. R_{eff} would be the FLUX_RADIUS with 50% of the light.

[c] CLASS_STAR is the SE output of a neural network classification based on the relative areas of nine isophotes in each object. It is only reliable for bright objects and becomes a random value between 0 and 1 for fainter ones (Bertin & Arnouts 1996).

[d] MAG_ISO, the total flux of all the pixels above the detection threshold. If the same pixels are selected in the other filter by using dual image mode, the resulting color is more indicative of the total object.

[e] The ratio of MU_MAX over MAG_BEST (SE's choice between MAG_ISO and MAG_AUTO depending on crowding) provides a additional concentration index.

[f] MAG_APER, the flux within the specified apertures (PHOT_APERTURES). The fluxes from the *V* and *I* catalogs are a color indicator. For the colors we use an aperture with a diameter of 3 and 5 pixels (0″15 and 0″25, respectively). This choice of small diameters was done to obtain a conservative color estimate with minimal contamination from neighboring objects in crowded fields.

TABLE 3
Source Extractor Output Parameters We Have Added

Name	Description	Used	Unit	Comments
CONCENTRATION	Abraham concentration parameter	*	...	a
CONTRAST..	Abraham contrast parameter	*	...	b
SQR_ASYMMETRY....................................	Point-asymmetry index (difference squared)		...	c
ASYMMETRY	Point-asymmetry index (absolute difference)	*	...	d
MAJOR_AXIS_ASYM	Major axis asymmetry index		...	e
MINOR_AXIS_ASYM	Minor axis asymmetry index		...	e
MOFFAT..	Computed Moffat magnitude		mag	f
MOFFAT_RMS..	Ratio rms deviation to computed Moffat flux		...	f
MOFFAT_RES..	Ratio absolute residue to computed Moffat flux		...	f

[a] CONCENTRATION is the fraction of light in the central 30% of the objects area, measured in an ellipse aligned with the object and having the same axis ratio. It is described in detail in Abraham et al. (1994). Adapted from code kindly provided by I. Smail.

[b] CONTRAST is the fraction of object's flux in the brightest 30% of the total number of pixels. Also from Abraham et al. (1994) and courtesy of I. Smail.

[c] SQR_ASYMMETRY $= \sum_i [(I_i - I_j)^2 / I_i + I_j]$, where I_j is the counterpart of I_i, equidistant with respect to the object's center and rotated over $180°$. Described in Conselice (1997) and adapted for SE by the authors.

[d] ASYMMETRY $= \sum_i |I_i - I_j| / I_i + I_j$, where I_j is the counterpart of I_i, equidistant with respect to the object's center and rotated over $180°$. Based on the expression in Conselice et al. (2000) and also incorporated into SE.

[e] MAJOR_AXIS_ASYM and MINOR_AXIS_ASYM are as ASYMMETRY, but the (x, y) position of I_i is mirror of the (x, y) position of I_j with respect to the major or minor axes, respectively.

[f] MOFFAT parameters: SE computes a Moffat profile $[I = I_0 / (1 + \alpha r^2)^\beta]$ from the peak pixel value (I_0) and the detection threshold [a known value of intensity (I) at a known distance (r) from the object's center]. We hoped that star clusters and foreground stars could be picked out of our catalogs using their similarity to a typical Moffat profile. However, confusion from blends prevented an easy selection. These parameters were not used in the computation of the Galaxy score.

Field galaxies missed by this procedure are not selected in either simulation or real data and therefore do not influence our comparison. There are, however, still some contaminant foreground objects that are selected as well, and these have to be identified and discarded by visual inspection.

3.4. Visual Identification of Contaminants

A human observer can pick out contaminants on the basis of contextual information not contained in the SE parameters.

There are five broad categories of remaining contaminants: star-clusters, diffraction spikes, H II regions, artifacts from dust lanes, and blended objects.

Stellar clusters, both young open clusters and globular clusters, are associated with the foreground galaxy. At the distance of the Virgo Cluster, these are often of approximately the size and color of more distant E0 field galaxies. Young open clusters are often found in spiral arms and are very blue, while globular
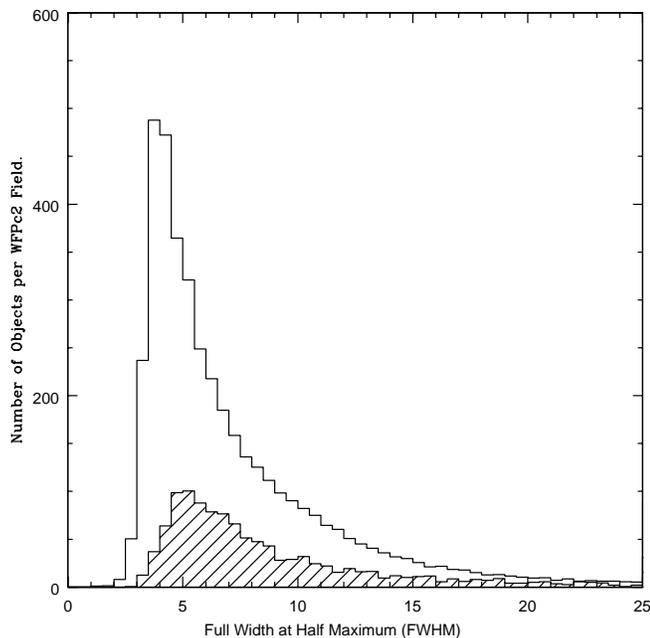

Fig. 3.—Distribution of the FWHM (in pixels), determined by SE, of all the objects in 21 of the science fields, averaged over the number of fields. The shaded area is the histogram per WFPC2 field for HDF galaxies (both north and south). A selection limit based on this parameter only would not have done nearly as well as our scoring system.
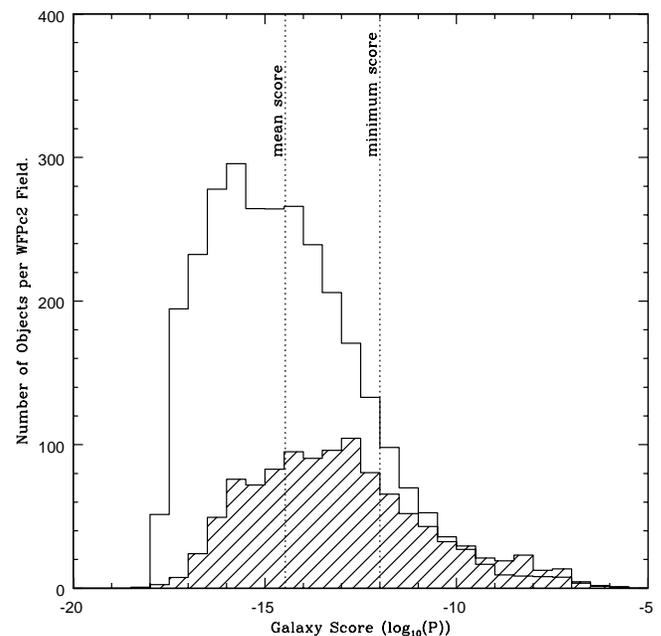

Fig. 4.—Distribution of galaxy score for objects in our science fields. $P = \prod P_i / [\prod P_i + \prod (1 - P_i)]$. The shaded area is the average histogram for HDF galaxies (both north and south). Objects to the right are more galaxy-like. The majority of field galaxies is indistinguishable in properties from the objects in the foreground galaxy. Only the higher scoring tail (about -12 and above) can be used for the opacity measurement. The mean score of all objects is indicated, together with the minimum score for selection.

TABLE 4
Visual Rejection Percentages

Galaxy	Total	Crowded	Arm	Interarm
NGC 4536............................	22	89	50	16
NGC 1365............................	35	100	56	19
NGC 1365 (A=2).................	55	97	66	31
Adopted rates	. . .	100	50	20

Note.—Average rejection percentages of added HDF objects in visual checks identical to those in the real fields, using all the zero extinction simulations. We use rejection fractions for the average synthetic field counts of 0.5 and 0.2 for arm and interarm regions, respectively, to correct the simulated numbers for the visual step on the real number of field galaxies.

clusters can be identified by the slightly different brightness profile. Bright stars in our own galaxy result in false selections. Their wings are extended, often blending with other objects, and the diffraction spikes resemble edge-on galaxies. The proximity of these false selections to the bright star makes them easily visually identifiable. H ii regions resemble blue irregular galaxies but are invariably found in the proximity of several blue open clusters. Dust lanes superposed on a smooth disk may result in an extended "object," which is often reddened. This results in severe contamination, especially in flocculant spiral galaxies, making their inner regions unsuitable for the SFM.

Blended objects are by far the largest source of contamination. A blend of one of the above objects with a small clump of stars is likely to be selected as a candidate field galaxy. In addition, in a nearby foreground galaxy, the granularity of the partly resolved disk may result in contamination from blended clumps of disk stars. SE performs deblending of the peaks in the flux, but the choice of parameters governing this is a trade-off between deblending objects and keeping extended objects intact. The candidate objects from the science fields were marked in the F814W image for visual inspection together with their score and color. Objects deemed to be contaminants were removed. All the candidates from the science fields are removed from the synthetic field candidate list.

However, the numbers of simulated galaxies have to be corrected for any false selections as a result of a blend of a faint HDF object and a foreground one. To correct the numbers from the simulated fields, the same visual check was done on the simulations from both galaxies with no artificial extinction ($A = 0$) and in the case of NGC 1365 also in an extincted simulation ($A = 2$). The candidate objects were in this case the real galaxies, the simulated galaxies, and the misidentifications, both from the original field and as a result from the addition of the HDF objects. The percentage of HDF objects rejected, mostly as blends, in these visual checks is given in Table 4 per typical region, an indicator of the measure of crowding. These percentages do not seem to change much as a function of either choice of galaxy or simulation. To correct for blends of HDF and foreground objects, a fixed percentage of the remaining simulated galaxies from a typical region is removed after the removal of the science field's candidates. These adopted percentages are also given in Table 4 for each typical region.

4. IMPROVEMENTS IN THE SYNTHETIC FIELD METHOD

In the process of automating the SFM we have introduced several improvements. First, exposures were combined with the drizzle routine, improving the sampling of the final image. Second, we have provided for a less observer-dependent selection

of field galaxies. These two categories of improvements we have described in the previous sections. Third, extra simulations were made, biases and uncertainties were estimated, and opacities were obtained on the basis of segments of the images with similar characteristics. We describe these improvements in this section.

4.1. Foreground Galaxy Segmention

The SFM provides an average opacity for a certain region of the foreground galaxy. Paper I reported opacities for regions defined by WFPC2 chip boundaries. Ideally, an average opacity is determined for a region of the foreground galaxy that is homogeneous in certain characteristics: arm or interarm regions, deprojected radius from the center of the galaxy, or a region with the same surface brightness in a typical band.

In our treatment, the mosaicked WFPC2 fields are visually divided into crowded, arm, interarm, and outside regions. This step is applied to the catalogs of objects by tagging each object according to its general location in the foreground galaxy. Objects from the crowded regions were ignored in the further analysis. The deprojected radial distance for each object was also computed from the inclination, position angle, and position of the galaxy center taken from the Two Micron All Sky Survey (2MASS) Large Galaxy Atlas (Jarrett et al. 2003) or, alternatively, from the extended source catalog (Jarrett et al. 2000); the distance was taken from Freedman et al. (2001). The surface brightness based on the *HST*/WFPC2 mosaics or a 2MASS image could also be used to define a partition of the WFPC2 mosaics.

4.2. Simulated Fields

Simulated fields are made by taking one WF chip from either the northern or southern HDF (HDF-N or HFD-S), extincting it with a uniform gray screen, and adding it to a data WF chip. This results in six separate simulations for each opacity and data chip: one for each HDF-N/S WF chip. Simulations for seven opacity levels were made, ranging from -0.5 to 2.5 mag of extinction with steps of 0.5 mag. The negative -0.5 opacity simulation was added to obtain a more accurate fix on the point of zero opacity. The use of a gray screen in the simulations was chosen because its effect on the numbers of field galaxies is similar to that of a distribution of dark, opaque clouds with a specific filling factor and size distribution.[7]

To infer the opacity (A_I) from the numbers of field galaxies (N), Paper I uses

$$A_I = -2.5C \log\left(\frac{N}{N_0}\right), \qquad (3)$$

where N_0 is the normalization and C the slope of the relation between the number of field galaxies and the extinction. They depend on the crowding in the field and total solid angle. Crowding limits the number of field galaxies. When it dominates the loss of field galaxies, the relation becomes much flatter ($C \gg 1$). Paper I found C to differ with the extinction law used in the simulations in the same foreground field. We use gray extinction but vary the foreground field.

For each field, we fit the relation between A_I and $\log N$, minimizing χ^2 to the average numbers of field galaxies found in

---

[7] Moreover, Paper I found that assuming a Galactic or a gray extinction curve made no difference in the extinction derived in NGC 4536 using the SFM.

the simulated fields with known extinctions.[8] The intersection of this curve with the real number of field galaxies yields an average opacity estimate for the region. See Figures 6, 9, 10, and 11 for the fitted relation (*dashed line*) and the number of field galaxies from the science field (*solid line*).

4.3. *Field Galaxy Numbers: Uncertainties and Systematics*

There are four quantities, besides dust absorption, that affect the numbers of field galaxies. They are crowding, confusion, counting error, and clustering. Crowding and confusion introduce biases that need to be calibrated. Counting and clustering introduce uncertainties in the galaxy numbers that must be estimated. In addition, the clustering could possibly introduce a bias if the reference field is not representative for the average. *Crowding* effectively renders the parts of the image of little use for the SFM. Typically, these are stellar clumps, the middle of spiral arms, and the center of the foreground galaxy. The strongly crowded regions in the WFPC2 mosaics were masked off and not used in further analysis. *Confusion* is the misidentification of objects by either the selection algorithm or the observer. Misidentification by the algorithm is corrected for by the visual check of the science fields (detailed in § 3.4). In order to correct the numbers of simulated objects, the candidates from the science field, including the misidentifications, are removed, and subsequently the average rejection rate from Table 4 is applied to the remaining objects from each typical region. The typical regions are a measure for the crowding, the main source of the remaining confusion due to blends of HDF and foreground objects.

Counting introduces a Poisson error. If the numbers are small ($N < 100$), $\sqrt{N}$ underestimates the error and the expressions by Gehrels (1986) for upper and lower limits are more accurate. We adopted these for both simulated and real galaxy numbers using the expressions for upper and lower limits for 1 standard deviation. *Clustering* introduces an additional uncertainty in the number of *real* galaxies in the science fields, as the background field of galaxies behind the foreground galaxy is only statistically known. This variance in the background field necessitates a prudent choice of reference field for the background in the simulated fields, as otherwise an inadvertent bias in the opacity measurement can be introduced (see also § 4.3.1).

The standard deviation of this uncertainty can be estimated using a similar argument to the one in Peebles (1980, p. 152), replacing volume by solid angle and the three-dimensional two-point correlation function by the two-dimensional one [$\omega(\theta)$]. The resulting clustering uncertainty depends on the depth of the observation and the solid angle under consideration:

$$\sigma_{\text{clustering}}^2 = N + N^2 \left[A(m_{\text{lim}}, \text{Filt}) \frac{2\Gamma(2 + \delta)}{\Gamma(2 + \frac{\delta}{2})\Gamma(3 + \frac{\delta}{2})} \theta_{\text{max}}^\delta \right],$$

$$(4)$$

where $A(m_{\text{lim}}, \text{Filt})$ is the amplitude, depending on photometric band and brightness interval, and δ is the slope of the two-point correlation function $\omega(\theta) = A\theta^\delta$. N is the number of field galaxies, and θ_{max} characterizes the size of the solid angle under consideration. The slope δ is usally taken to be -0.8, and the value of the term between $A(m_{\text{lim}}, \text{Filt})$ and $\theta_{\text{max}}^\delta$ in equation (4)

TABLE 5
EXTINCTIONS FOR DIFFERENT REGIONS IN THE FIELDS

Region	A_I[a]	ΔA_c[b]	$A_I \cos(i)$[c]
NGC 1365			
WFPC2	$0.5^{+0.3}_{-0.3}$	(± 0.3)	$0.4^{+0.3}_{-0.3}$
Arm (II)	$3.9^{+2.6}_{-3.5}$	(± 1.8)	$3.2^{+2.2}_{-2.9}$
Arm (IV)	$-0.7^{+1.1}_{-1.1}$	(± 0.8)	$-0.6^{+0.9}_{-0.9}$
Interarm (III)	$0.4^{+0.6}_{-0.6}$	(± 0.4)	$0.3^{+0.5}_{-0.5}$
Outside (V)	$0.5^{+0.4}_{-0.4}$	(± 0.3)	$0.4^{+0.3}_{-0.3}$
$R(0.2-0.4)$	$2.8^{+2.4}_{-2.9}$	(± 1.6)	$2.3^{+2.0}_{-2.4}$
$R(0.4-0.5)$	$0.6^{+0.6}_{-0.7}$	(± 0.4)	$0.5^{+0.5}_{-0.5}$
$R(0.5-0.6)$	$0.4^{+0.6}_{-0.7}$	(± 0.4)	$0.3^{+0.5}_{-0.5}$
$R(0.6-1.0)$	$0.2^{+0.4}_{-0.4}$	(± 0.3)	$0.2^{+0.3}_{-0.3}$
NGC 4536			
WFPC2	$0.9^{+0.4}_{-0.4}$	(± 0.3)	$0.4^{+0.2}_{-0.2}$
WF2, 3	$0.9^{+0.7}_{-0.8}$	(± 0.5)	$0.4^{+0.3}_{-0.4}$
WF4	$0.9^{+0.6}_{-0.7}$	(± 0.4)	$0.4^{+0.3}_{-0.4}$
$R(0.4-0.6)$	$0.4^{+0.6}_{-0.6}$	(± 0.4)	$0.2^{+0.3}_{-0.3}$
$R(0.6-0.7)$	$1.1^{+0.9}_{-1.0}$	(± 0.6)	$0.5^{+0.4}_{-0.5}$
$R(0.7-0.8)$	$1.6^{+1.0}_{-1.3}$	(± 0.7)	$0.7^{+0.5}_{-0.6}$
$R(0.8-1.0)$	$0.9^{+0.7}_{-0.8}$	(± 0.5)	$0.4^{+0.3}_{-0.4}$

NOTE.—Extinction measures in the different regions in the WFPC2 mosaics, uncorrected and corrected for the inclinations from Table 6.
[a] Opacities from $A_I = -2.5C \log(N/N_0)$, errors are the 1 σ uncertainties, including the clustering uncertainty in the number of galaxies from the science field.
[b] The contribution to the total error in opacity (ΔA_I) owing to galaxy clustering uncertainty in the background.
[c] The opacity and errors corrected for inclination.

becomes 1.44. The $A(m_{\text{lim}}, \text{Filt})$ values from Cabanac et al. (2000) are used to compute $\omega(\theta)$ and the resulting clustering uncertainty, as they are for the same filters (V and I) and integrated over practical brightness intervals with a series of limiting depths.[9] Paper I claims a completeness of galaxy counts up to 24 mag for one of the fields it covers. We estimate the limiting magnitude by the value above which 90% of the simulated galaxies with no dimming ($A = 0$) lie. We extrapolated the relation between limiting magnitude and amplitude [$A(m_{\text{lim}}, \text{Filt})$] from Cabanac et al. (2000) to model the clustering error to higher limiting magnitudes. For each field we characterise the limiting depth by the interval in which the majority of simulated field galaxies lie in the simulations with no opacity. Alternatively, we could have used a very large number of background fields in the simulations and determined the possible spread in field galaxy numbers due to clustering from those. For practical reasons we used the average of simulations with the HDF-N/S fields and estimated the uncertainty in the real number of field galaxies from equation (4). The uncertainties in opacity owing to the clustering uncertainty in the original background field are given separately in Table 5 and in Figures 6, 9, 10, and 11.

The clustering error and Gehrels's counting uncertainties were added in quadrature to arrive at the upper and lower limits of uncertainty for the real galaxies. Simulated counts only have a counting uncertainty, as these are from a known typical background field.

From the errors in the number of field galaxies in each simulation and in the real number of field galaxies, the uncertainty in the average opacity A can then be derived from equation (3). A single field gives a highly uncertain average value for extinction. Averaging over several galaxies improves statistics and mitigates the error from field galaxy clustering.

4.3.1. *The HDF as a Reference Field*

The SFM uses the HDFs as backgrounds in the synthetic fields. The counts from these are taken to be indicative of the average counts expected from a random piece of sky suffering from the same crowding issues as the original field. In this use of the HDF-N/S as the reference field, the implicit assumption is that it is representative of the average of the sky. If they are not, the difference in source counts between the HDFs and the average sky introduces a bias in the synthetic fields and hence a bias in the resulting opacity measure.

The position of the HDF-N was selected to be unremarkable in source counts and away from known nearby clusters (Williams et al. 1996). The position of the HDF-S was dictated by the need to center the Space Telescope Imaging Spectrograph on a QSO, but Williams et al. (2000) assert that the source count in HDF-S was unlikely to be affected by that. In addition, Casertano et al. (2000) point out that the HDF-S was chosen such that it was similar in characteristics to HDF-N. The selection strategy of the HDFs therefore does not seem to be slanted toward an overdensity of sources.

To test the degree to which the HDFs are representations of the average field of sky, the numbers of galaxies we find can be compared with numbers from the Medium Deep Survey (Griffiths et al. 1994), a program of parallel observations with the WFPC2, also in F814W. Several authors (Casertano et al. 1995; Driver et al. 1995a, 1995b; Glazebrook et al. 1995; Abraham et al. 1996a; Roche et al. 1997) report numbers of galaxies as a function of brightness in these fields. Casertano et al. (1995), Driver et al. (1995a), Glazebrook et al. (1995), Abraham et al. (1996a), and Roche et al. (1997) present averages for multiple fields, and Driver et al. (1995b) and Abraham et al. (1996a) the numbers from deep fields, the latter for the HDF-N. In Figure 5, we plot these numbers of galaxies as a function of magnitude. In addition, the number of sources identified by our algorithm as field galaxies in the HDFs are also plotted. The average of the HDFs (*filled circles*) corresponds well to the curves from the literature up to our practical limiting depth of 24 mag. The difference between the north and south HDF never exceeds the Poisson uncertainty of the average and even changes sign for galaxies fainter than 24 mag.

From Figure 5, we conclude that the average of the HDFs is a good representation of the average field in the sky, and the numbers of galaxies from the simulations do not need to be corrected for any bias resulting from an atypical reference field. In any case, any residual bias would be trivial compared with the uncertainties in individual WFPC2 fields, although they could have become important when combining counts from many fields, as we have done in our companion paper (Paper IV).

4.4. *Inclination Correction*

Any inclination correction of the opacity values depends on the assumed dust geometry. A uniform dust screen in the disk would result in a factor of $\cos(i)$ to be applied to the opacity A_I. However, if the loss of field galaxies is due to a patchy distribution of opaque dust clouds, the correction becomes dependent on the filling factor, cloud size distribution, and cloud oblateness. All the extinction estimates (A_I) and the values
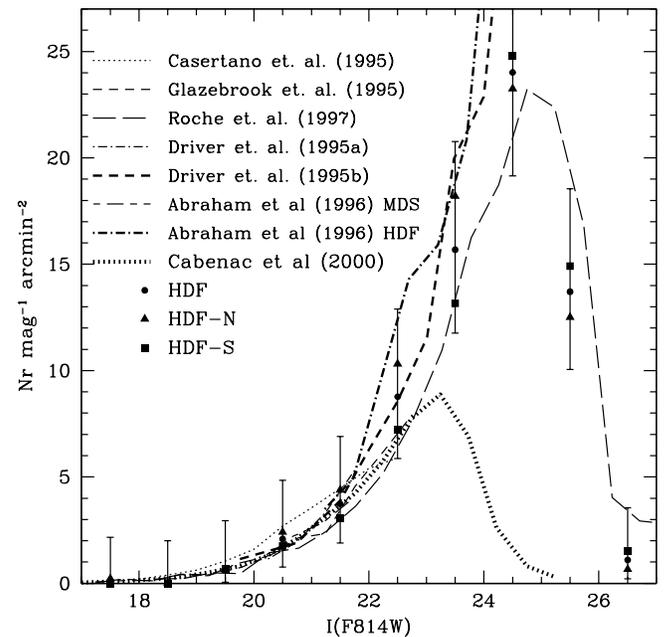

FIG. 5.—Numbers of field galaxies per magnitude per square arcminute from several authors. All counts were in the *I* band (F814W). The HDF points are the average of all our counts for HDF-N and HDS-S. Triangles and squares are our averages for HDF-N and HDF-S, respectively. The numbers by Casertano et al. (1995) are from prerefurbished WFPC data, accounting for the slightly higher numbers. The numbers found by Abraham et al. (1996b) for the HDF-N are slightly higher than ours for the fainter objects, as our selection started to discard some. The dashed lines are from single deep WFPC2 exposures (Driver et al. 1995b; Abraham et al. 1996a), the solid lines from multiple exposures (Casertano et al. 1995; Glazebrook et al. 1995; Driver et al. 1995a; Abraham et al. 1996a, 1996b; Roche et al. 1997).

corrected for inclination [$A_I \cos(i)$] are listed in Table 5, assuming a simple uniform dust screen.

5. EXAMPLES: NGC 4536 AND NGC 1365

NGC 4536 (Paper I) was reanalyzed as a test case to provide a comparison between observers and versions of the SFM. NGC 1365 was one of the first galaxies analyzed with the improved method (Holwerda et al. 2002b) and provides a good example of how the method works for an image that can be segmented into different regions. See Table 6 for basic data on both galaxies and the observations that made up the data set.

5.1. *NGC 4536: Comparing Observers*

Identifying field galaxies remains a subjective process, and different software systems, as well as different observers, will differ in their identifications. However, as long as the same selection criteria are applied to simulations and science objects, a good estimate of dust extinction can be made. Figure 6 shows the extinction measurements from Paper I and this paper.

The numbers of field galaxies and subsequent derived opacities in the combined WF2 and 3 chips are very similar for Paper I and this paper. The results for WF4 seem to differ, however, both in numbers of field galaxies found and the derived extinction. WF4 was analyzed separately by Paper I, as it was less crowded than the other two WFPC2 chips, so field galaxies could be found to a higher limiting depth. Paper I estimates the limiting magnitude for the WF4 chip to be 24 mag and for the WF2 and 3 field to be 23 mag. The selection of objects as candidate field galaxies by our algorithm, however, imposes a

| GALAXY | TYPE | PROPOSAL ID | EXPOSURE TIME | | DISTANCE[a] (Mpc) | R_{25}[b] (kpc) | INCLINATION[c] (deg) |
			V_{F555W}	I_{F814W}			
NGC 1365.................................	SBb	5972	66,560.0	16,060.0	17.95	27.3	34
NGC 4536.................................	SAB(rs)bc	5427	68,000.0	20,000.0	14.93	16.5	63

[a] All distances were taken from Freedman et al. (2001).
[b] The 25 *B* magnitude surface brightness radius from RC3.
[c] Derived from the reported axis ratio (*sup_ba*) in the 2MASS Large Galaxy Atlas (Jarrett et al. 2003).

limiting depth to which objects are selected ($I \approx 23$ mag). This effect can be seen in the cumulative histogram of real galaxies (Fig. 7), especially in the WF4, where the numbers from Paper I continue to increase beyond 24 mag. The effect is less pronounced in the simulated numbers (Fig. 7, *bottom right*). These differences in numbers at the faint end are the cause of the difference in derived opacities for Paper I and this paper. How-

ever, a lower limiting magnitude makes the derived extinction less accurate (lower number statistics and a bigger uncertainty due to clustering) not inconsistent with each other.

If the numbers from Paper I are limited to the same limiting magnitude as ours, the numbers from science and simulated fields galaxies match up. In addition, in a visual check, both observers agree on the identification of these brighter field
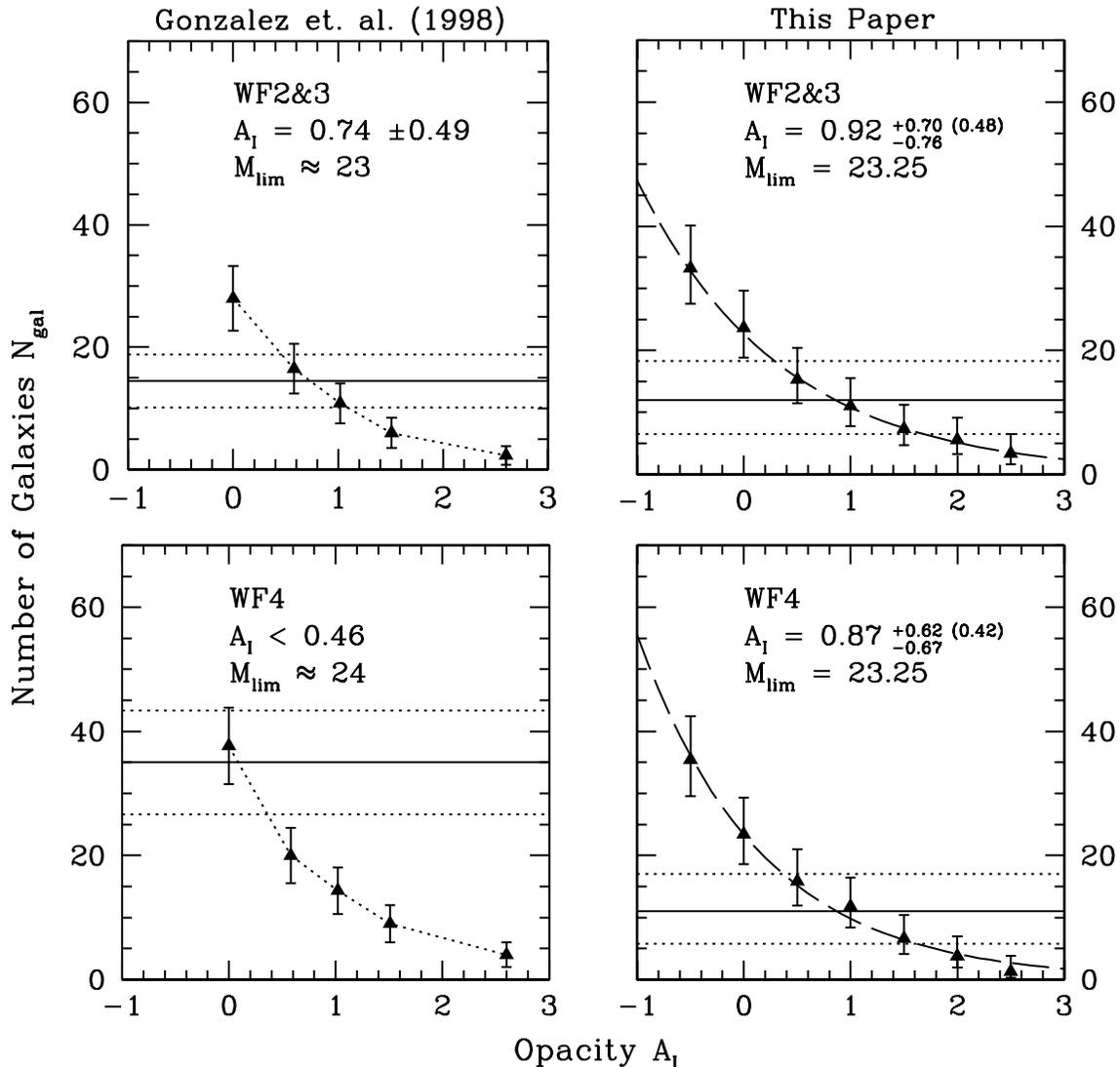
FIG. 6.—Number of simulated galaxies per WF chip as a function of extinction for the Paper I result (*left*) and this paper (*right*). The top panels are the average for WF2 and 3, combined by Paper I because of their similar appearance and poor statistics. The bottom panels are WF4. The error bars for the simulated numbers (*triangles*) are Poisson uncertainties only. The dashed line is the best fit [$A_I = -2.5C \log (N/N_0)$]. The solid horizontal line is the real number of field galaxies found; the dotted horizontal lines mark the uncertainty in this number due to counting and clustering combined. The opacity measurement shows also the total error and that part of the error due to clustering in brackets. The limiting magnitude M_{lim} was determined from the $A = 0$ simulation.
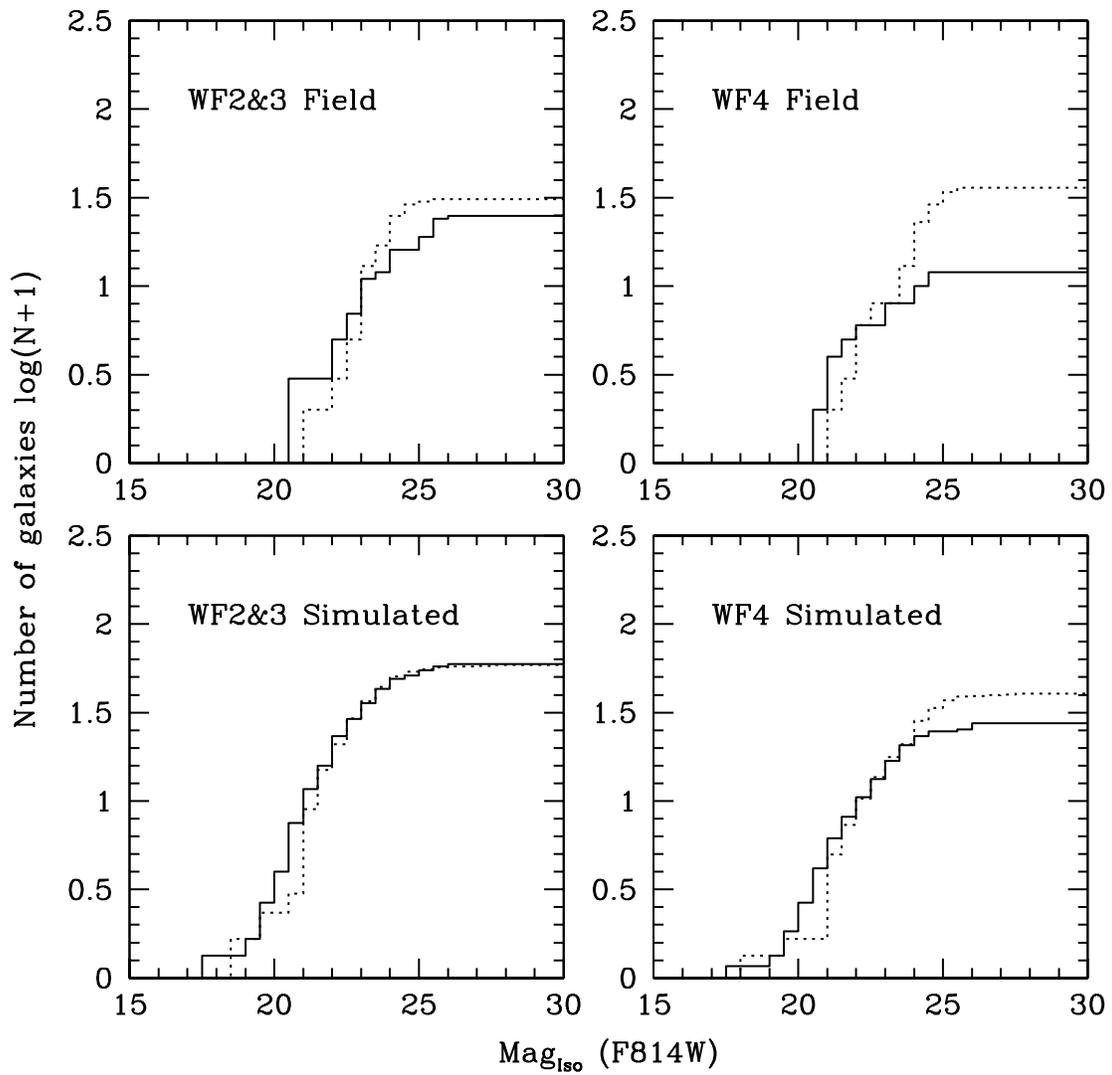
FIG. 7.—Cumulative histograms of the number of field galaxies with their magnitude (MAG_ISO) for our identifications (*solid lines*) and those of Paper I (*dotted lines*) for WF2 and 3 (*left*) and WF4 (*right*); science field galaxies (*top*); simulated field galaxies (*bottom*).
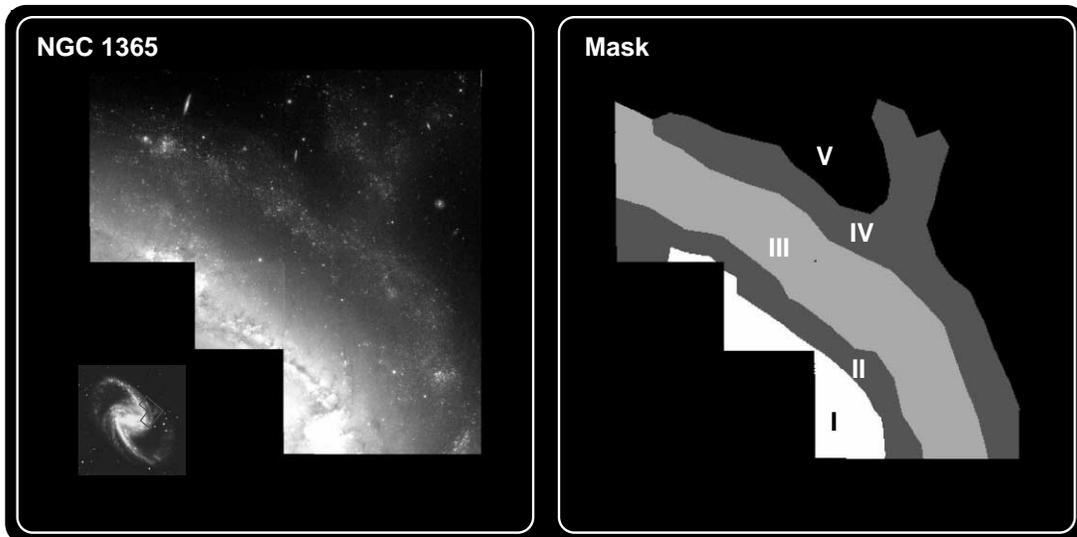

FIG. 8.—Mask used to denote crowded (I), arm (II, IV), interarm (III), and outside (V) regions in NGC 1365. Galaxy number counts are given for the inner arm region (II), interarm region (III), the spur (IV), and the outside region (V) in Fig. 9.
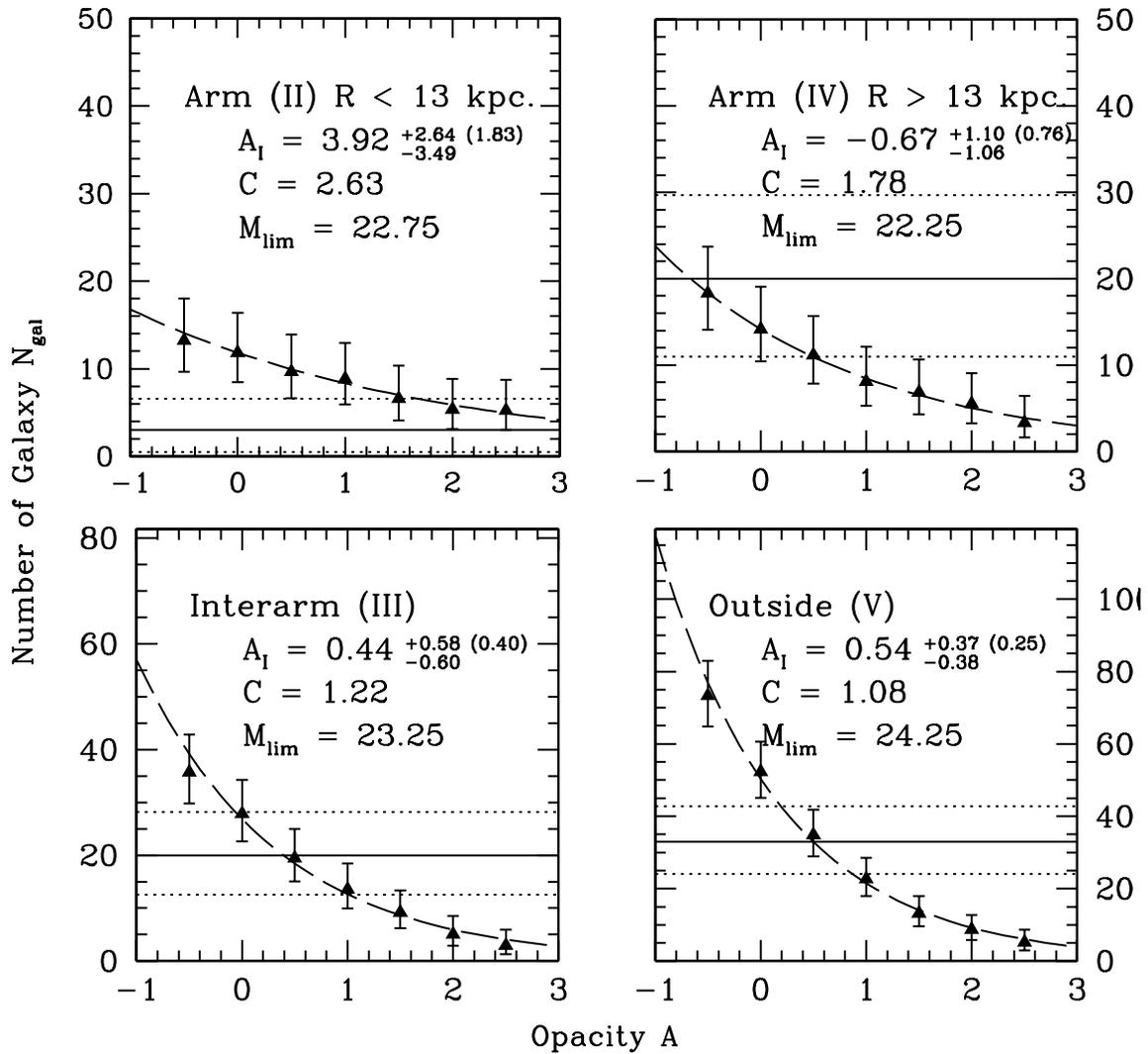
Fig. 9.—Simulated and real numbers of field galaxies in typical regions in NGC 1365; arm regions on either side of the interarm region (region II and IV in Fig. 7), the interarm region (region III), and the outside region (region V). Error bars, notation, and curves are the same as the right panels in Fig. 6. C is the fit for eq. (3). M_{lim} is the limiting magnitude used to compute the clustering uncertainty.

galaxies. Given this, we feel that the automated method's trade of depth for speed is warranted.

By automatically selecting objects and correcting the simulations for the pruning of galaxies in the visual step, we are confident that we select similar sets of field galaxies, to the same limiting depth, with a high degree of certainty in both simulated and real fields.

5.2. *NGC 1365: Arm and Interarm Extinction*

Paper I remarked on the importance of distinguishing between arm regions, regions between the arms (interarm), and outside regions. Beckman et al. (1996), White et al. (2000), and Domingue et al. (2000) all found that extinction was more concentrated in the spiral arms. NGC 1365 provides a nice example of an arm with a crowded region, an interarm region, a spur, and some outside area (see Fig. 8). The opacity measurements of these regions are plotted in Figure 9. The spur region (IV), the interarm region (III), and the region outside (V) show some opacity, but all are still consistent with none. Most of the extinction in this galaxy is in the main inner arm (II): $A = 3.9^{+2.6}_{-3.5}$. For such a small subdivision in only one field, this opacity measure is very uncertain. However, by combining

measurement in several arm regions in several galaxies, as we have done in Paper IV, we are confident that a reliable and meaningful estimate can eventually be made.

5.3. *NGC 4536 and NGC 1365: Radial Profile of Extinction*

One of the new applications of the SFM introduced here is to compare the numbers of field galaxies in an annular region of the mosaic between two deprojected radii. Figures 10 and 11 show results for four sets of annuli for NGC 4536 and NGC 1365, respectively. We present the radial opacity values found in this way in Figure 12 for both NGC 4536 and NGC 1365. Noticeable is the occurrence of comparatively high values of opacity at different radii. This depends on whether or not the area in the radial annulus is dominated by arm regions or interarm-type regions.

The NGC 1365 profile shows a steep rise in the inner region, and the peak in the NGC 4536 profile corresponds to the prominent arm there. Individual errors in these measurements remain quite large because of the poor statistics and the clustering uncertainty in the field of galaxies.

Comparing these values with those in Figure 12 of White et al. (2000), the peak values in these radial plots, at 0.3 and
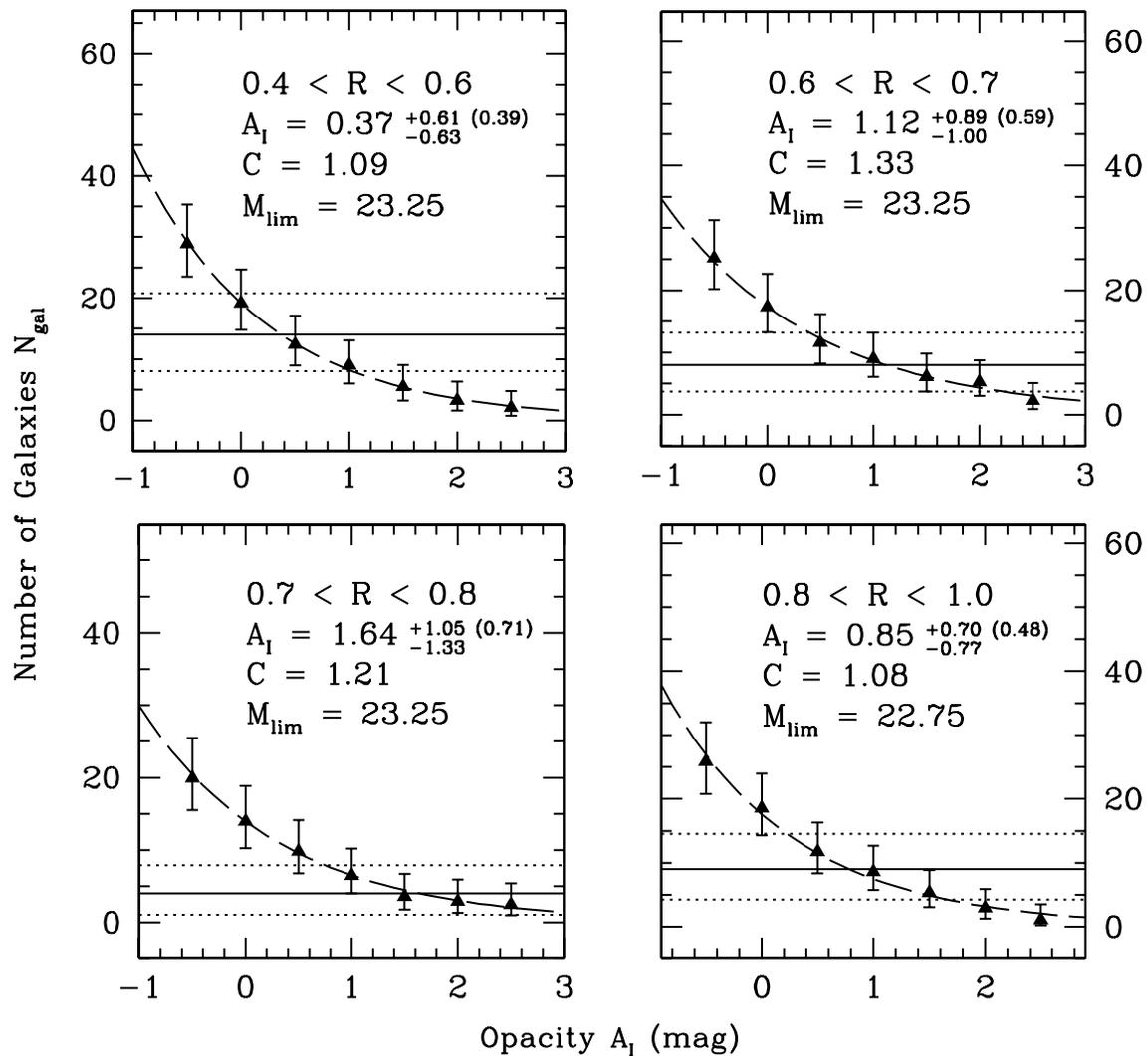
FIG. 10.—Numbers of real field galaxies and those of simulated field galaxies plotted as a function of simulated opacity in areas of deprojected radius from the center of NGC 4536. The radii are expressed in R_{25}, derived from the B-band photometric diameter (D_{25}) from de Vaucouleurs et al. 1991 (RC3). Error bars, notation, and curves are the same as the right panels in Fig. 6. C is the fit for eq. (3). $M_{\lim}$ is the limiting magnitude used to compute the clustering uncertainty.

0.75R_{25}, respectively (see Fig. 12), are completely consistent with the arm extinction values found by those authors. When combining the radial profiles of our entire sample of *HST* fields, we should keep in mind the importance of spiral arms in the radial extinction profile.

5.4. *Surface Brightness*

Giovanelli et al. (1995), Tully et al. (1998), and Masters et al. (2003) found that disk extinction correlates with total galaxy luminosity. With the SFM we can have a more detailed look at the correlation between the light in a galaxy and the extinction. The higher extinction found in spiral arms is an indication that this correlation is also present in our data. However, with few points obtained from only two fields, no relation can be reliably detected. A plot of the extinctions and surface brightnesses derived from all our fields will be presented in a future paper.

6. CONCLUSIONS

We have shown that the SFM as developed by Paper I can be successfully automated and applied to a large variety of fields. As most classification schemes break down in crowded regions,

some visual check by a human observer remains necessary, either to deem the region too crowded or to check the classification of the objects. The bias thus introduced is also calibrated using synthetic fields. The great increase in throughput provided by the automation opens up the possibility to infer dust absorption in a wide range of fields available in the *HST* archive.

In the process of automating the SFM, we introduced some improvements. The quality of the images has been improved with the drizzle technique. The selection of field galaxies is less observer dependent and much faster. Extra HDF-S control fields were added to mimic the average background field. The results are now given per typical region instead of per chip. Improved estimates of the uncertainties due to the random error and the clustering of the field galaxies have also been incorporated.

Future improvements of this technique could include the use of multicolor imaging or field spectroscopy in order to more unambiguously identify the field galaxies. An improved object classification, based on different data and with a more sophisticated algorithm, could in the future make the need for a visual check of objects redundant.

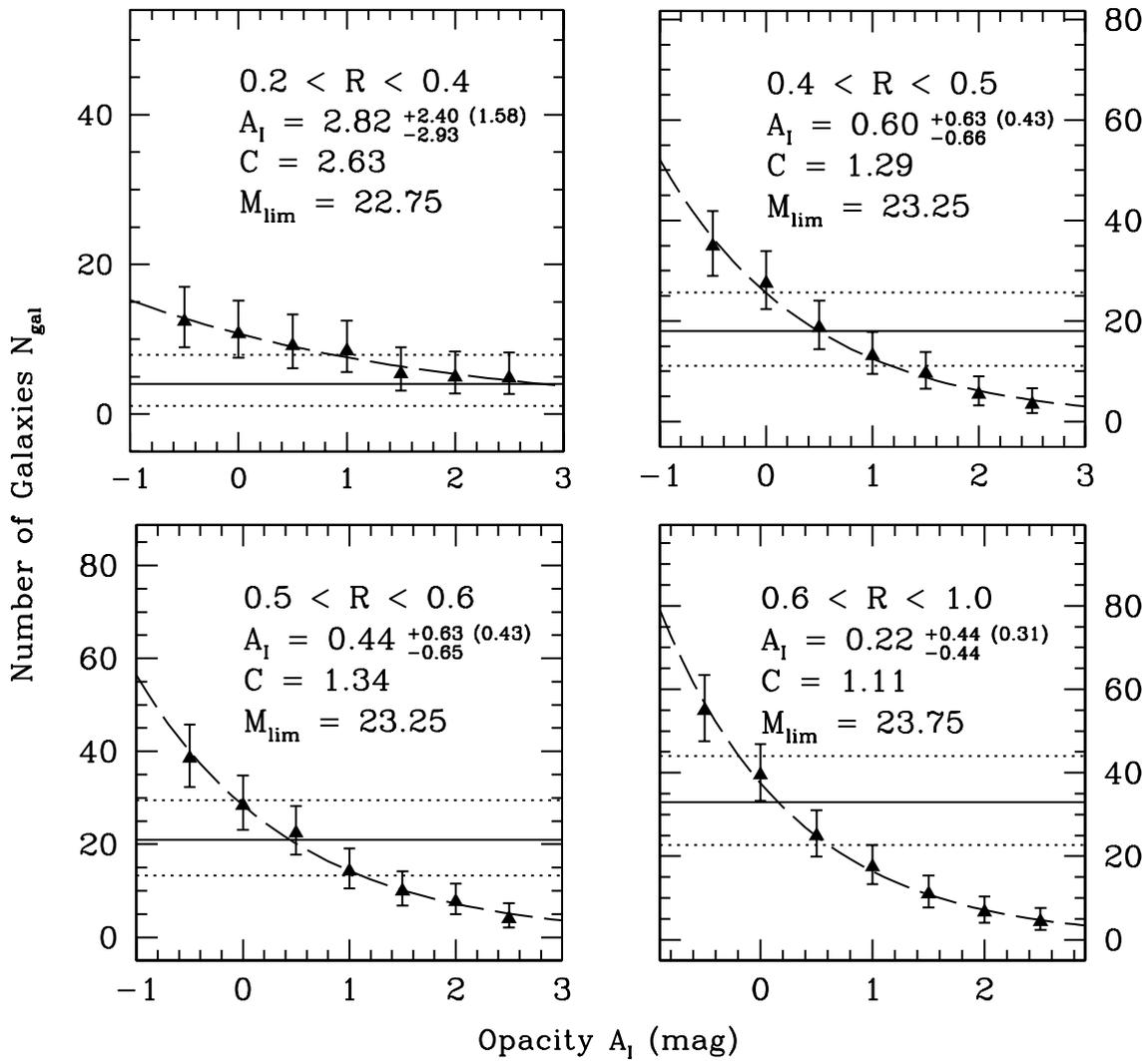The apparent difference between derived extinctions between this paper and Paper I for NGC 4536 can be accounted

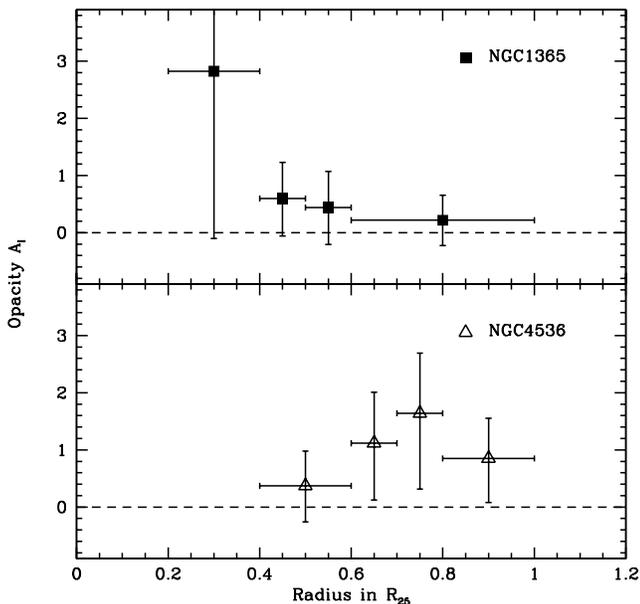FIG. 11.—Same as Fig. 10, but for NGC 1365.

FIG. 12.—Dust extinction plotted as a function of radius, expressed in R_{25}. The opacity of NGC 1365 (*top*) for the entire field, with all radii combined, is $A = 0.5^{+0.3}_{-0.3}$, and for NGC 4536 (*bottom*), the opacity of the entire field, is $A = 0.9^{+0.4}_{-0.4}$.

for by a difference in limiting depth and the uncertainty it brings with it. However, the agreement between observers in their identifications of the brighter objects suggests a consistency of the method across identification schemes.

The radial dependencies of opacity in our examples show evidence of substantial extinction, $A_I = 0.6^{+0.6}_{-0.7}$ mag for NGC 1365 at half the R_{25} and $A_I = 1.6^{+1.0}_{-1.3}$ at $0.75R_{25}$ radii for NGC 4536. These extinction values at these radii are consistent with those reported by White et al. (2000). Most of this extinction seems to concentrate in the arm regions of these galaxies.

While the SFM itself is independent of assumptions about the dust geometry in the foreground galaxy, the inclination correction for the opacity is not. Corrections based on a simple screen have been presented, and a more thorough discussion of other possibilities is considered in the companion paper (Paper IV).

The principal advantage of this method is that no assumption about the distribution of either absorbers or the underlying starlight goes into the measurement. However, the small number statistics in individual regions result in large uncertainties for single measurements. Averages over several fields will improve this by increasing the statistics and averaging out the field galaxy clustering. The application of this method to a substantial set of archival *HST*/WFPC2 images is presented in Paper IV.

REFERENCES

Abraham, R. G., Tanvir, N. R., Santiago, B. X., Ellis, R. S., Glazebrook, K., & van den Bergh, S. 1996a, MNRAS, 279, L47
Abraham, R. G., Valdes, F., Yee, H. K. C., & van den Bergh, S. 1994, ApJ, 432, 75
Abraham, R. G., van den Bergh, S., Glazebrook, K., Ellis, R. S., Santiago, B. X., Surma, P., & Griffiths, R. E. 1996b, ApJS, 107, 1
Andredakis, Y. C., & van der Kruit, P. C. 1992, A&A, 265, 396
Beckman, J. E., Peletier, R. F., Knapen, J. H., Corradi, R. L. M., & Gentet, L. J. 1996, ApJ, 467, 175
Berlind, A. A., Quillen, A. C., Pogge, R. W., & Sellgren, K. 1997, AJ, 114, 107
Bershady, M. A., Jangren, A., & Conselice, C. J. 2000, AJ, 119, 2645
Bertin, E., & Arnouts, S. 1996, A&AS, 117, 393
Burstein, D., & Heiles, C. 1982, AJ, 87, 1165
Cabanac, R. A., de Lapparent, V., & Hickson, P. 2000, A&A, 364, 349
Casertano, S., Ratnatunga, K. U., Griffiths, R. E., Im, M., Neuschaefer, L. W., Ostrander, E. J., & Windhorst, R. A. 1995, ApJ, 453, 599
Casertano, S., et al. 2000, AJ, 120, 2747
Conselice, C. J. 1997, PASP, 109, 1251
———. 1999, Ap&SS, 269, 585
———. 2003, ApJS, 147, 1
Conselice, C. J., Bershady, M. A., & Jangren, A. 2000, ApJ, 529, 886
Cuillandre, J., Lequeux, J., Allen, R. J., Mellier, Y., & Bertin, E. 2001, ApJ, 554, 190
Davies, J. I., & Burstein, D. 1995, The Opacity of Spiral Disks (Dordrecht: Kluwer)
de Vaucouleurs, G., de Vaucouleurs, A., Corwin, H. G., Jr., Buta, R. J., Paturel, G., & Fouqué, P. 1991, Third Reference Catalogue of Bright Galaxies (New York: Springer) (RC3)
Disney, M. 1990, Nature, 346, 105
Domingue, D. L., Keel, W. C., Ryder, S. D., & White, R. E. 1999, AJ, 118, 1542
Domingue, D. L., Keel, W. C., & White, R. E. 2000, ApJ, 545, 171
Driver, S. P., Windhorst, R. A., & Griffiths, R. E. 1995a, ApJ, 453, 48
Driver, S. P., Windhorst, R. A., Ostrander, E. J., Keel, W. C., Griffiths, R. E., & Ratnatunga, K. U. 1995b, ApJ, 449, L23
Dutra, C. M., Bica, E., Clariá, J. J., Piatti, A. E., & Ahumada, A. V. 2001, A&A, 371, 895
Elmegreen, D. M., Kaufman, M., Elmegreen, B. G., Brinks, E., Struck, C., Klarić, M., & Thomasson, M. 2001, AJ, 121, 182
Freedman, W. L., et al. 2001, ApJ, 553, 47
Gehrels, N. 1986, ApJ, 303, 336
Giovanelli, R., Haynes, M. P., Salzer, J. J., da Costa, L. N., & Freudling, W. 1995, AJ, 110, 1059
Glazebrook, K., Ellis, R., Santiago, B., & Griffiths, R. 1995, MNRAS, 275, L19
González, R. A., Allen, R. J., Dirsch, B., Ferguson, H. C., Calzetti, D., & Panagia, N. 1998, ApJ, 506, 152 (Paper I)

González, R. A., Loinard, L., Allen, R. J., & Muller, S. 2003, AJ, 125, 1182
Greenfield, P., & White, R. L. 2000, ASP Conf. Ser. 216, Astronomical Data Analysis Software and Systems IX, ed. N. Manset, C. Veillet, & D. Crabtree (San Francisco: ASP), 59
Griffiths, R. E., et al. 1994, ApJ, 435, L19
Gurwell, M., & Hodge, P. 1990, PASP, 102, 849
Hodge, P. W. 1974, ApJ, 192, 21
Holwerda, B. W., Allen, R. J., & van der Kruit, P. C. 2001, BAAS, 33, 1390
———. 2002a, in ASP Conf. Ser. 273: The Dynamics, Structure, and History of Galaxies, G. S. Da Costa & H. Jerjen (San Francisco: ASP), 337
Holwerda, B. W., Allen, R. J., van der Kruit, P. C., & Gonzalez, R. A. 2002b, BAAS, 34, 1292
Holwerda, B. W., Gonzalez, R. A., Allen, R. J., & van der Kruit, P. C. 2005, AJ, 129, 1396 (Paper IV)
Hubble, E. 1934, ApJ, 79, 8
Jablonka, P., Bica, E., Bonatto, C., Bridges, T.-J., Langlois, M., & Carter, D. 1998, A&A, 335, 867
Jarrett, T. H., Chester, T., Cutri, R., Schneider, S., & Huchra, J. P. 2003, AJ, 125, 525
Jarrett, T. H., Chester, T., Cutri, R., Schneider, S., Skrutskie, M., & Huchra, J. P. 2000, AJ, 119, 2498
Keel, W. C., & White, R. E. 2001a, AJ, 121, 1442
———. 2001b, AJ, 122, 1369
Koekemoer, A. 2002, *HST* Dither Handbook, Version 2.0 (Baltimore: STScI)
Lequeux, J., Dantel-Fort, M., & Fort, B. 1995, A&A, 296, L13
MacGillivray, H. T. 1975, MNRAS, 170, 241
Masters, K. L., Giovanelli, R., & Haynes, M. P. 2003, AJ, 126, 158
Mutchler, M., & Fruchter, A. 1997, BAAS, 29, 1271
Peebles, P. J. E. 1980, The Large-Scale Structure of the Universe (Princeton: Princeton Univ. Press)
Roche, N., Ratnatunga, K., Griffiths, R. E., & Im, M. 1997, MNRAS, 288, 200
Roennback, J., & Shaver, P. A. 1997, A&A, 322, 38
Sebok, W. L. 1979, AJ, 84, 1526
Shane, C. D., & Wirtanen, C. A. 1967, Publ. Lick Obs., 22, 1
Shapley, H. 1951, Proc. Natl. Acad. Sci., 37, 133
Swam, M. S., & Swade, D. A. 1999, in ASP Conf. Ser. 172, Astronomical Data Analysis Software and Systems VIII, ed. J. I. Davies, C. Impey, & S. Phillipps (San Francisco: ASP), 203
Tully, R. B., Pierce, M. J., Huang, J., Saunders, W., Verheijen, M. A. W., & Witchalls, P. L. 1998, AJ, 115, 2264
Valentijn, E. A. 1990, Nature, 346, 153
Wesselink, A. J. 1961, MNRAS, 122, 503
White, R. E., & Keel, W. C. 1992, Nature, 359, 129
White, R. E., Keel, W. C., & Conselice, C. J. 2000, ApJ, 542, 761
Williams, R. E., et al. 2000, AJ, 120, 2735
———. 1996, AJ, 112, 1335
Zaritsky, D. 1994, AJ, 108, 1619